Crossover Scaling of Wavelength Selection in Directional Solidification of Binary Alloys

Michael Greenwood, Mikko Haataja, and and Nikolas Provatas

Department of Materials Science and Engineering, and Brockhouse Institute for Materials Research, McMaster University, 1280 Main Street West, Hamilton, Ontario, Canada, L8S 4L7

(Received 10 April 2004; published 6 December 2004)

We simulate cellular and dendritic growth in directional solidification in dilute binary alloys using a phase-field model solved with adaptive-mesh refinement. The spacing of primary branches is examined for a wide range of thermal gradients and alloy compositions and is found to undergo a maximum as a function of pulling velocity, in agreement with experimental observations. We demonstrate that wavelength selection is unambiguously described by a nontrivial crossover scaling function from the emergence of cellular growth to the onset of dendritic fingers. This result is further validated using published experimental data, which obeys the same scaling function.

DOI: 10.1103/PhysRevLett.93.246101 PACS numbers: 68.70.+w, 05.70.Ln, 64.70.Dv, 81.30.Fb

In the process of casting, solidification often occurs as a competitive growth of dendritic arrays. A paradigm used in the study of competitive dendritic growth is two dimensional (2D) directional solidification. In this process a binary alloy in a thin film geometry is solidified through a fixed temperature gradient G, with the cooling rate controlled by a pulling speed V. After becoming unstable via the Mullins-Sekerka (MS) instability [1] the solidification front develops complex dendritic patterns. The morphology of dendritic structures controls the microstructure and solute segregation of the solidified alloy.

Directional solidification has been well characterized both experimentally [2–10] and theoretically [11–16]. Theories for predicting length scale selection in dendritic arrays often use geometrical arguments that relate the tip shape to the fastest linearly unstable wavelength, which is related to the process parameters [3,11,17]. While some predictions are in qualitative agreement with experimental trends [17], they display a quantitative discrepancy from experiments. Theoretical predictions are often validated by fitting data over certain ranges of pulling velocity [4]. Such procedures can be seriously hampered by the limited range of data or crossover effects [4].

Crossover phenomena can be attributed to a competition between two or more physical mechanisms operating on different scales. The crossover can be captured by employing a technique known as scaling. One first attempts to isolate the material/process-dependent scales, and the behavior of the system emerges as a collapse of the data that has been properly nondimensionalized by these scales. Scaling occurs in phenomena such as surface growth [18], critical phenomena [19], and dendritic growth [20]. The attractive feature of the scaling approach is that it quantitatively describes the behavior of the system over many different regimes.

In this Letter, we examine wavelength selection in directional solidification. We use a phase-field model solved on an adaptive grid [21,22], allowing system sizes several orders larger than the diffusion length and greatly reducing simulation time. We show that primary spacing as a function of velocity for our simulated data and published experimental data [4] is described by a crossover scaling function across the *entire* range from the emergence of cellular growth into the dendritic regime.

Directional solidification was simulated using a phase-field model for solidification presented in [23]. For the case of unequal solid/liquid diffusivities, it uses an antitrapping flux to eliminate spurious kinetic and interface stretching terms when recovering the corresponding sharp-interface model in the limit when the interface thickness is smaller than the characteristic scale of the microstructure. This is an extension to the sharp-interface asymptotics that recover the sharp-interface model in the limit of vanishing interface thickness [24]. The model describes solidification of a dilute binary alloy with a partition coefficient k. It couples an order parameter ϕ to a concentration field C. The field $\phi(\vec{x})$ takes on the values $\phi = 1$ in the solid phase, $\phi = -1$ in the liquid phase and interpolates continuously between these states in the interface region. In this formulation the equations of motion for the two fields are given by

$$\frac{\partial C}{\partial t} = -\nabla \cdot \vec{j} \tag{1}$$

and

$$A^2(\vec{n})\frac{\partial \phi}{\partial t} = \vec{\nabla} \cdot [A^2(\vec{n})\vec{\nabla}\phi] + \phi(1-\phi^2) - \frac{\lambda}{1-k}(e^{\mu} + \theta - 1)(1-\phi^2)^2 + \frac{1}{2}\vec{\nabla} \cdot \left[|\nabla\phi|^2 \frac{\partial A^2(\vec{n})}{\partial(\vec{\nabla}\phi)} \right], \tag{2}$$

where $e^{\mu} = 2(C/C_l^0)/[1 + k - (1-k)\phi]$ and the so-called *antitrapping* flux $\vec{j} = -DCq(\phi)\nabla u - a_t C_l^0(1-k)e^{\mu}(\partial_t\phi)\vec{n}$ with $\vec{n} = \nabla\phi/|\nabla\phi|$, the unit normal to the contours of ϕ. In the above, space has been rescaled by W_0, the interface width, time by τ_0, the interface kinetics time and C_0^l is the liquid phase alloy concentration. The

dimensionless temperature is defined by a *frozen field* $\theta = (1-k)(z-V_p t)/l_T$, where z is the pulling direction, $l_T = |M_L|(1-k)C_0^l/(W_0 G\lambda)$ is the thermal length, and G the dimensional thermal gradient. This is justified since the ratio of thermal to mass diffusion in typical alloys is of order 10^4 [25]. The pulling velocity $V_p = V_s\tau/W$, where V_s is the dimensional pulling speed. The constant M_L is the liquidus slope. The concentration and phase fields are coupled via the constant λ. The dimensionless diffusion constant is $D = D_L\tau_0/W_0^2$ where D_L is the diffusion constant in the liquid which sets the diffusion length $l_D = 2D/V_p$. Two-sided diffusion is controlled by the function $q(\phi) = (1-\phi)/[1+k-(1-k)\phi] + (1+\phi)\xi/2$ where $\xi = D_s/D_L = 10^{-4}$. Surface tension anisotropy is defined in terms of $\vec{n}$. Specifically, $A(\vec{n}) = [1-3\epsilon_4]\{1+(4\epsilon_4/1-3\epsilon_4)[(n_x)^4+(n_y)^4]\}$, where ϵ_4 is the anisotropy constant. The anisotropic interface width is thus defined as $W(\vec{n}) = W_0 A(\vec{n})$ and the characteristic time $\tau(\vec{n}) = \tau_0 A^2(\vec{n})$ [21–23,26]. Anisotropy appears in both τ and W in order to be able to make interface kinetics term $\beta = 0$ in the sharp-interface limit.

The constants W_0, τ_0, λ and the antitrapping flux coefficient a_t are inter-related by an asymptotic analysis [23], which maps the phase-field model onto the sharp-interface limit defined by: (1) solute diffusion in the bulk phases, (2) flux conservation at phase-boundaries and (3) the Gibbs-Thomson condition $C_{\text{int}} - C_{\text{eq}} = -d(\vec{n})\kappa - \beta(\vec{n})V$, with κ the local interface curvature, $d(\vec{n}) = d_0[A(\vec{n}) + \partial^2 A/\partial(\cos^{-1}n_x)^2]$ where d_0 is the isotropic capillary length and V is the normal interface speed. Attaining the limit $\beta = 0$ requires $d_0/W \approx 0.8839/\lambda$, $D \approx 0.6267\lambda$, and $a_t = 1/(2\sqrt{2})$. Similar thermodynamically consistent formulations are also possible for low cooling rates [27].

The phase-field model was simulated in 2D using a finite element method on an adaptive grid, with zero-flux boundary conditions in both C and ϕ [21,22]. Solidification is initiated by a small amplitude, randomly perturbed solid-liquid interface. The initial solute profile $C(\vec{x}, 0)$ was set to a steady-state diffusion profile normal to the interface, while $\phi(\vec{x}, 0) = \tanh[\vec{x}/\sqrt{(2)}]$ along the normal to the interface. All system sizes considered were in the range of 6400 to 12800 in the z direction and varied from 1600–6400 in the transverse direction. The minimum grid spacing was set to $dx_{\min} = 0.39$ in all cases. We used explicit time integration, with a time step $dt = 0.008$ as in Ref. [23]. The anisotropy $\epsilon_4 = 0.0025$, which is close to that of PVA. We have shown elsewhere that our results are essentially unchanged for smaller $dx_{\min}$ in the case of both explicit [22] and implicit [20] time integration, and that our numerical methodology is robust to rotations of our lattice by an angle of $\pi/4$ [22].

We simulated directional solidification using the following three sets of parameters (G, λ, C_0^l, k): (0.00191, 20, 0.13 mol%, 0.16), (0.0015, 3, 1.5 mol%, 0.15), and (0.002, 1.3, 1.5 mol%, 0.15). Upon setting $D_L = 6.0 \times 10^{-10}$ m^2/s and $d_0 = 2.12 \times 10^{-8}$ m, appropriate for PVA-ACE, W_0 and τ_0 are given by $W_0 = (4.0 \times 10^{-7}$ m; 6.05×10^{-8} m; 3.1×10^{-8} m), and $\tau_0 = (3.3 \times 10^{-3}$ s; 1.14×10^{-5} s; 1.3×10^{-6} s), set by the parameter inter-relationships discussed above. We note that using $\lambda = 20$ enabled us to obtain data close to the planar-to-cellular onset boundary. As the pulling velocity V_p (oriented parallel to the surface tension anisotropy) was varied we observed cellular structures at low values of V_p, while at high velocities we observed the emergence of dendritic morphologies, as shown in Fig. 1. The microstructure interface was analyzed using a power spectral analysis as in [28]. The primary branch spacing λ_1 was obtained by examining the power spectrum, $P_q = \langle |h_q|^2 \rangle$, of the solid-liquid interface profile as a function of time. The main peak position, which corresponds to the visually observed primary spacing λ_1, was computed using the definition $k_{\text{mean}} = (\sum_{q>0} q P_q / \sum_{q>0} P_q) \equiv 2\pi/\lambda_1$. The value k_{mean} was plotted versus $1/t$ and extracted to $1/t \to 0$ to obtain an estimate of λ_1. Data for k_{mean} vs $1/t$ is shown in the insets of Fig. 1 for two different morphologies.

Figure 2 shows the primary branch spacing λ_1 vs V_P for our computed data. For two of our data sets a maximum occurs in λ_1 as V_p approaches the planar-cellular onset. Furthermore, we found that this maximum value occurs at V_p^* satisfying $l_T \approx l_D$. The presence of such a maximum has been predicted theoretically [17] and observed in several experiments [2,4]. The data from Ref. [4] are shown in the inset of Fig. 2. The three experiments shown are for SCN-0.25 mol% Salol at $G = 13$ K/mm, SCN-0.13 mol% ACE at $G = 13$ K/mm, and PVA-0.13 mol% ethanol at

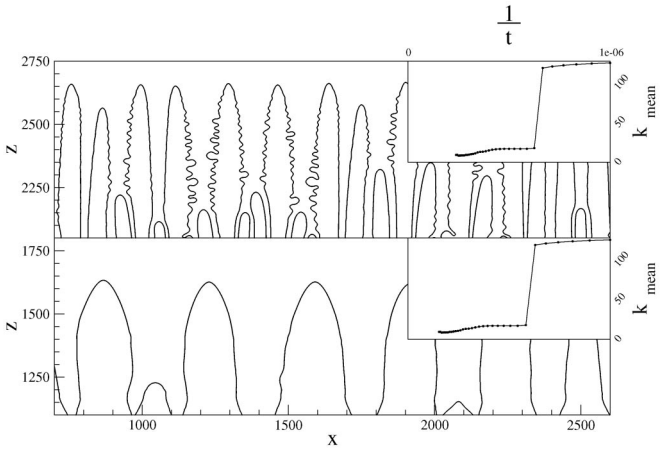

FIG. 1. (bottom) Typical cellular structures for $V_s = 150$ μm/s and $G = 1500$ K/mm. (top) Dendritic morphology with sidebranch structures corresponding to $V_s = 90$ μm/s and $G = 10$ K/mm. The insets show k_{mean} versus inverse time. Units are in terms of the interface width W_0.

$G = 18.5\,\mathrm{K/mm}$. For $V_p > V_p^*$, the data in Fig. 2 displays the characteristic monotonically decreasing wavelength as a function of velocity.

There has been a great deal of work on scaling relationships for primary branch spacing in different morphological regimes ([8], and references therein). These typically take the form $\lambda_1 = A l_T^{\alpha} l_D^{\beta} d_0^{\gamma}$. The prefactor and exponents α, β, and γ can vary depending on the semiempirical and/or geometrical arguments of a given theory [3,8,17]. Moreover, the scaling form must necessarily assume distinct exponents when different growth regimes are present [3].

We describe the primary branch selection through a crossover scaling function of the form

$$\frac{\lambda_1}{\lambda_c} = \frac{l_T}{l_D} f\left(\frac{l_T}{l_D} - \frac{l_T}{l_D^*}\right), \tag{3}$$

where λ_c is the onset steady-state wavelength at the transition from the planar-to-cellular instability and $l_D^* \equiv 2D/V_c$, where V_c is the velocity at the onset. Figure 3 shows our computed data collapsed onto a scaling function of the form above. Also shown on the scaled plot is the experimental data from Refs. [3,4]. In each case λ_c was selected so as to obtain the best data collapse by plotting $\Lambda \equiv (\lambda_1 l_D)/(\lambda_c l_T)$ against $(l_T/l_D - l_T/l_D^*)$. The plot is remarkable in that it predicts a scaling function describing the primary spacing (λ_1) versus velocity over a wide range of pulling speeds, thermal gradients, alloy concentrations, and materials. The crossover function in Fig. 3 covers the regime from cellular fingers and crosses over into the dendritic regime.

Figure 4 compares our values of λ_c to $\lambda_{\mathrm{theory}} = \sqrt{\lambda_{\mathrm{ms}} l_{\mathrm{TR}}(V_p = V_c)}$, where λ_{ms} denotes the MS wavelength at the planar-to-cellular onset boundary ($V_p = V_c$), and $l_{\mathrm{TR}}(V_p)$ is a velocity-dependent generalization of l_T, implicitly determined from $l_{\mathrm{TR}} = l_T[1 - \exp(-l_{\mathrm{TR}} V_p/D)]$. Physically, $l_{\mathrm{TR}}(V_p)$ is proportional to the amplitude of cellular fingers such that $l_{\mathrm{TR}} \approx l_T[1 - l_D^*/(2l_T)]$ at the onset of cellular growth, while in the opposite limit ($V_p \gg V_c$), $l_{\mathrm{TR}} \to l_T$. This form of $\lambda_{\mathrm{theory}}$ is similar to a previous analytical prediction of λ_c derived geometrically by approximating the tip shape and calculating the tip undercooling [17]. In the same figure we compare our extracted λ_c to another theoretical prediction, $\lambda_{\mathrm{theory}} = (d_0 l_D l_T)^{1/3}$, the geometric mean of the three length scales, empirically suggested to be proportional to the wavelength at the planar-to-cellular onset [8]. Figure 4 suggests that for both cases $\lambda_c = \alpha\lambda_c(1 + \beta d_0/\lambda_{\mathrm{theory}})$, where α and β are material independent constants. These results imply that $\lambda_c \propto \lambda_{\mathrm{theory}}$ at large wavelengths. At small wavelengths, analytic predictions differ from our findings. This is likely due to the fact that fitting an arm to an ellipsoid of revolution is only true at large wavelengths.

We also examined the tip undercooling Δ_{tip} as a function of pulling velocity as in Ref. [29]. We found that Δ_{tip} decreases monotonically toward a plateau value for the largest V_p simulated. The reason is that at low V_p the diffusion length increases as the thermal length $l_{\mathrm{TR}}(V_p)$ decreases, not allowing the tip to escape its impurities. The front thus falls back from the pulling gradient, increasing Δ_{tip}. As V_p increases, $l_{\mathrm{TR}}(V_p)$ increases toward l_T, while l_D decreases. In this regime the interface is free to catch up to the pulling gradient, decreasing Δ_{tip}. As V_p

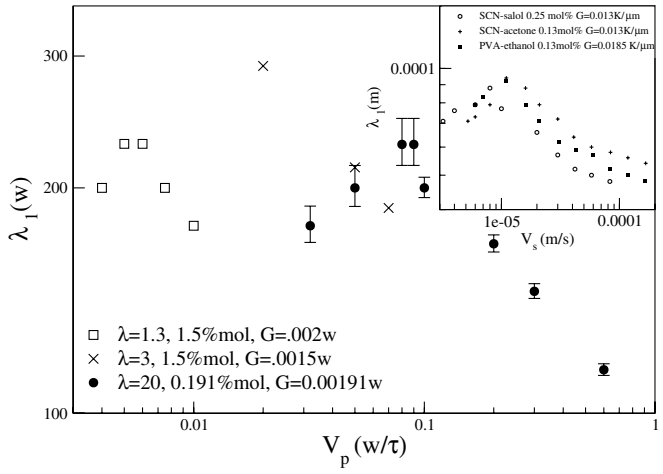

FIG. 2. Computed primary spacings corresponding to parameters listed in the text, error bars included for a single data set. The inset shows experimental primary spacing data obtained by digitizing data from Ref. [4].

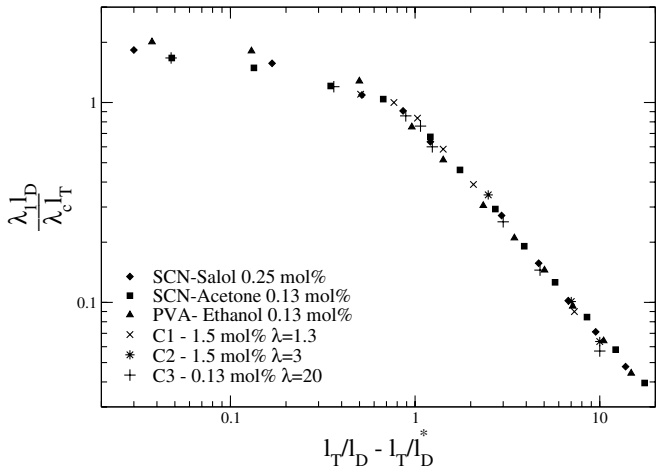

FIG. 3. Computed data and experiments [3,4] for SCN and PVA scaled to material properties, producing a single scaling function for the primary branch spacing λ_1

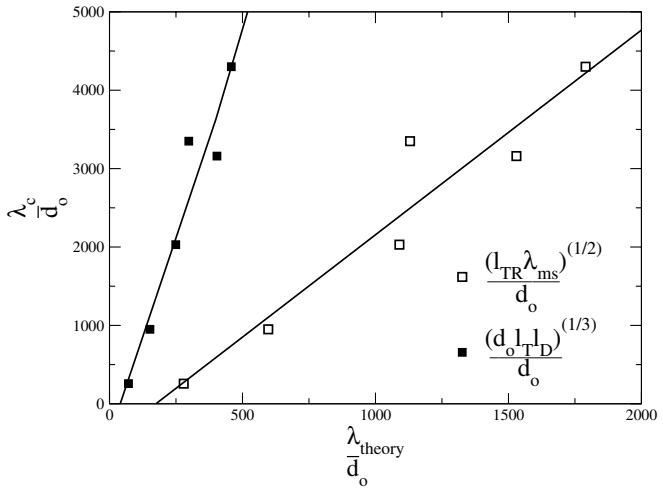

FIG. 4. A plot of λ_c/d_0 versus $\sqrt{\lambda_{ms} l_{TR}(V_c)}$ (lower line), and $(d_0 l_D l_T)^{1/3}/d_0$ (steeper line).

increases further we expect the undercooling to further increase, eventually reaching the dendritic-to-planar boundary as l_D approaches d_0 [30].

Our scaling function describes wavelength selection in directional solidification with the anisotropy parallel to the growth direction. We have explicitly demonstrated this in 2D, and expect to find scaling collapse in 3D by repeating our procedure. We also expect the scaling function to be very robust with respect to changes in the solid diffusivity and/or magnitude of surface tension anisotropy, as they simply renormalize V_c and λ_c. As an extension of this work, we are currently investigating the scaling behavior of cellular growth as the pulling direction is tilted away from the surface tension anisotropy direction; in this case, competition between the thermal gradient and surface tension anisotropy can lead to complicated spatiotemporal structures known as ''seaweeds,'' as demonstrated recently in experiments [10] and simulations [16].

To summarize, we have simulated wavelength selection of cellular patterns in 2D directional solidification using the phase-field method solved on an adaptive grid. The selected wavelength displays nonmonotonic behavior as a function of pulling speed; in particular, it displays a maximum for intermediate values of pulling speed. Our scaling function shows the collapse of both our computed data and previously published experimental data [4] onto a single crossover scaling function. We strongly believe that the scaling approach undertaken in the present work can be further extended into a predictive tool for microstructure selection in solidification processing of binary and multicomponent alloys.

We would like to thank the Center for Automotive Materials and Manufacturing at McMaster University for financial support, and SHARC-NET for supercomputer time.

[1] W.W. Mullins and R.F. Sekerka, J. Appl. Phys. **34**, 323 (1963).
[2] J. Bechhoefer and A. Libchaber, Phys. Rev. B **35**, 1393 (1987).
[3] J.S. Kirkaldy, L.X. Liu, and A. Kroupa, Acta Metall. Mater. **43**, 2905 (1995).
[4] L.X. Liu and J.S. Kirkaldy, Acta Metall. Mater. **43**, 2891 (1995).
[5] W. Losert, O.N. Mesquita, J.M.A. Figueiredo, and H.Z. Cummins, Phys. Rev. Lett. **81**, 409 (1998).
[6] W. Losert, B.Q. Shi, and H.Z. Cummins, Proc. Natl. Acad. Sci. U.S.A. **95**, 431 (1998).
[7] W. Losert, B.Q. Shi, and H.Z. Cummins, Proc. Natl. Acad. Sci. U.S.A. **95**, 439 (1998).
[8] R. Trivedi and W. Kurz, Acta Metall. Mater. **42**, 15 (1994).
[9] R. Trivedi and K. Somboonsuk, Mater. Sci. Eng. **65**, 65 (1983).
[10] B. Utter, R. Ragnarsson, and E. Bodenschatz, Phys. Rev. Lett. **86**, 4604 (2001).
[11] M.H. Burden and J.D. Hunt, J. Cryst. Growth **22**, 109 (1974).
[12] S.R. Coriell, G.B. McFadden, and R.F. Sekerka. Annu. Rev. Mater. Sci. **15**, 119 (1985).
[13] B. Grossmann, K. Elder, M. Grant, and M. Kosterlitz, Phys. Rev. Lett. **71**, 3323 (1993).
[14] D.A. Kessler and H. Levine, Phys. Rev. A **39**, 3041 (1989).
[15] N. Provatas and J. Dantzig, *The Enyclopedia of Materials Science and Technology* (World Scientific, Oxford, 2001).
[16] N. Provatas, Q. Wang, M. Haataja, and M. Grant, Phys. Rev. Lett. **91**, 155502 (2003).
[17] W. Kurz and D.J. Fisher, Acta Metall. **29**, 11 (1981).
[18] A.-L.Barabasi and H.E. Stanley, *Fractal Concepts in Surface Growth* (Press Syndicate of the University of Cambridge, New York, 1995).
[19] Nigel Goldenfeld, *Lectures on Phase Transitions and the Renormalization Group* (Addison-Wesley, Reading, MA, 1992).
[20] N. Provatas, N. Goldenfeld, J. Dantzig, J.C. LaCombe, A. Lupulescu, M.B. Koss, M.E. Glicksman, and R. Almgren, Phys. Rev. Lett. **82**, 4496 (1999).
[21] N. Provatas, J. Dantzig, and N. Goldenfeld, Phys. Rev. Lett. **80**, 3308 (1998).
[22] N. Provatas, J. Dantzig, and N. Goldenfeld, J. Comput. Phys. **148**, 265 (1999).
[23] A. Karma, Phys. Rev. Lett. **87**, 115701 (2001).
[24] A.A. Wheeler, W.J. Boettinger, and G.B. McFadden, Phys. Rev. A **45**, 7424 (1992).
[25] J.S. Langer, Rev. Mod. Phys. **52**, 1 (1980).
[26] A. Karma and W.-J. Rappel, Phys. Rev. E **53**, 3017 (1996).
[27] K.R. Elder, Martin Grant, Nikolas Provatas, and Mike Kosterlitz, Phys. Rev. E **64**, 021604 (2001).
[28] D. Jasnow and J. Vinals, Phys. Rev. A **41**, 6910 (1990).
[29] S. Akamatsu, G. Faivre, and T. Ihle, Phys. Rev. E **51**, 4751 (1995).
[30] J.-M. Flesselles, A.J. Simon, and A.J. Libchaber, Adv. Phys. **40**, 1 (1991).